Physics of Fluids

Coalescence speed of two equal-sized nanobubbles

Cite as: Phys. Fluids **32**, 123304 (2020); https://doi.org/10.1063/5.0030406
Submitted: 22 September 2020 . Accepted: 06 November 2020 . Published Online: 02 December 2020

Eric Bird, Jun Zhou (周峻), and Zhi Liang (梁智)

AIP Publishing

Physics of Fluids ARTICLE scitation.org/journal/phf

Coalescence speed of two equal-sized nanobubbles

Cite as: Phys. Fluids 32, 123304 (2020); doi: 10.1063/5.0030406
Submitted: 22 September 2020 • Accepted: 6 November 2020 •
Published Online: 2 December 2020

Eric Bird,[1] Jun Zhou (周峻),[2] and Zhi Liang (梁智)[1,a)]

AFFILIATIONS

[1]Department of Mechanical Engineering, California State University, Fresno, California 93740, USA
[2]Department of Mechanical Engineering, Pennsylvania State University, The Behrend College, Erie, Pennsylvania 16510, USA

[a)]**Author to whom correspondence should be addressed:** zliang@csufresno.edu

ABSTRACT

In this work, we use molecular dynamics (MD) simulations coupled with continuum-based theoretical analysis to study the coalescence dynamics of two equal-sized nanobubbles (NBs). We first derive a governing equation for the evolution of the capillary bridge radius between two coalescing NBs from the axisymmetric Navier–Stokes equation. To verify the prediction from the governing equation, we carry out MD simulations of the coalescence of two NBs in a Lennard-Jones fluid system and directly measure the bridge radius, r_b, as a function of time, t. By varying the bubble diameter, we change the NB Ohnesorge number from 0.46 to 0.33. In all cases, we find the theoretical prediction overestimates the expansion speed of the capillary bridge at early time of NB coalescence. However, once we take into account the curvature-dependent surface tension and restrict the minimum principal radius at the capillary bridge to the size of the atom in the model liquid, the theoretical prediction agrees with the MD data very well in both early time and later time of the coalescence process. From the theoretical model, we find neither liquid viscous force nor liquid inertial force dominates at later time of coalescence of the model NBs. In this case, the MD simulation results show $r_b(t) \propto t^{0.76 \pm 0.04}$ with the scaling exponent considerably higher than that in the scaling law $r_b(t) \propto t^{0.5}$ for the viscous and inertial dominated regimes. The diameter ratio of fully merged NB to that of the original NB is about $\sqrt{2}$, which is different from $\sqrt[3]{2}$ for the coalescence of millibubbles and microbubbles.

I. INTRODUCTION

Nanobubbles (NBs) are gas-filled cavities in liquids with diameters ranging from tens to hundreds of nanometers. The key difference between NBs and ordinary macrobubbles is that macrobubbles rise rapidly to the surface of a liquid due to buoyancy and then burst, while the buoyancy effect on NBs is insignificant compared to Brownian motion. As a result, NBs can remain suspended in liquids for hours or even days.[1] The highly stable NBs have a higher possibility than macrobubbles to attach to or nucleate on the hydrophobic surfaces of fine/ultrafine particles.[2,3] As fine/ultrafine particles approach, the NBs on the adjoining surfaces can coalesce and form a gas bridge, which results in an attractive capillary force between two particle surfaces. The attractive force brings the two surfaces into contact and leads to aggregation of fine/ultrafine particles. The aggregated fine particles are easier to be captured by macrobubbles, which will provide sufficient buoyancy forces to elevate particles to the surface of liquid. A number of recent experimental studies have reported a significant increase of the flotation rate of fine/ultrafine particles in the presence of NBs.[4–6] Based on this mechanism, NBs have great potential in a broad range of applications, such as flotation of fine/ultrafine mineral particles[4,7,8] and removal of fats, oil, grease, and suspended solids from wastewater, clothes, and recycled paper.[2,3,9,10]

Since the coalescence between two NBs is the key process of many NB applications, a fundamental understanding of coalescence dynamics of NBs is essential for more efficient use of NBs in various industrial applications. While the coalescence dynamics of millibubbles and microbubbles has been widely studied through experiments,[11–15] the experimental study of the coalescence of NBs is very challenging due to the lack of detection tools that can image the ns-timescale dynamics of NBs in real time with nanoscale spatial resolution. Since the experimental investigation of NB coalescence is currently challenging, it is not clear if the existing theories on coalescence dynamics of bubbles, which have been shown to be accurate in the description of coalescence dynamics of

millibubbles and microbubbles,[11–15] are still applicable to the coalescence of NBs.

To address the aforementioned challenges, we resort to molecular dynamics (MD) simulations coupled with continuum-based theoretical analysis to study the coalescence dynamics of NBs. In MD simulations, one can track trajectories, velocities, and forces of all atoms and molecules in the model system by numerical integration of Newton's equation of motion. From the local fluid density or local intermolecular potential energy obtained from MD simulations, one can readily distinguish liquid and gas phases and determine the real-time geometry of the capillary bridge between two coalescing NBs. Therefore, MD simulations can be considered as numerical experiments, which allow us to study the microscopic details of NB coalescence dynamics that are inaccessible by current experimental means. MD simulations have been used to study the nucleation, growth, and movement of NBs on solid surfaces.[16–19] We will use MD simulations to study the coalescence dynamics of NBs. To avoid the merging of two NBs through the Ostwald ripening,[20] we focus on the coalescence dynamics of two equal-sized NBs in this work.

From experimental and numerical studies on the coalescence of millibubbles and microbubbles, different dynamic regimes for bubble coalescence have been identified.[14] The main objective of this work is to determine the expansion speed of the capillary bridge between coalescing NBs and identify the dynamic regimes of NB coalescence. To achieve this goal, we will monitor the capillary bridge radius r_b as a function of time t from MD simulations and compare the MD simulation results to the theoretical predictions derived from the Navier–Stokes (NS) equation. Furthermore, the magnitude of inertial and viscous stresses in the liquid surrounding the coalescing NBs can be directly calculated from the theoretical model. If the NB coalescence is in a dynamic regime that is dominated by either viscous or inertial stresses in liquid, the continuum-based theoretical model has predicted the scaling laws for capillary bridge expansion.[14,21] From the comparison between MD simulation results and theoretical predictions, we will determine if the coalescence dynamics of NBs can be still accurately described by the existing theories.

The rest of the paper is organized as follows: in Sec. II, we first derive the governing equation for the evolution of the capillary bridge between two coalescing NBs. From the governing equation, we further derive the scaling laws for $r_b(t)$ if the bubble coalescence is dominated by viscous or inertial stresses. In Sec. III, we describe the MD model used for the study of the coalescence of two equal-sized NBs and the properties of the model fluid obtained from MD simulations. In Sec. IV, we present MD simulation results. By comparing the simulation results to theoretical predictions, we will identify the dynamic regime of NB coalescence and discuss the accuracy of continuum-based theoretical predictions in NB coalescence. Finally, we close with conclusions.

II. THEORY

A. The governing equation for coalescence dynamics of NBs

When two equal-sized NBs touch each other, a capillary bridge forms between two NBs and expands in the radial direction. Figure 1 shows a schematic of two equal-sized NBs of radius R with

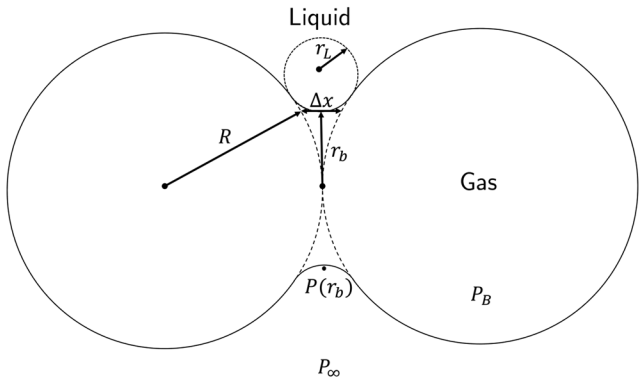

FIG. 1. Schematic of two equal-sized NBs coalescing in a liquid, where R is the radius of the NB, r_b is the radius at the capillary bridge minimum, Δx is the gap between two NBs measured in the equivalent configuration before coalescence, r_L is the principal radius at the bridge minimum on the liquid side, P_B is the pressure of gas within the NB, P_∞ is the pressure in the liquid far from the NB, and $P(r_b)$ is the liquid pressure near the bridge minimum.

a formed capillary bridge of radius r_b. The coalescence of NBs is characterized by the expansion speed of the capillary bridge. Using the method similar to the derivation of the Rayleigh–Plesset equation,[13] we derive the governing equation for the time evolution of the capillary bridge radius r_b from the axisymmetric NS equation. The symmetric axis passes through the center of the two coalescing NBs, as represented in Fig. 1.

1. Mass conservation

From the geometry shown in Fig. 1, the gap $\Delta x(r_b)$ between two NBs measured in the equivalent configuration before coalescence is given by

$$\Delta x(r_b) = 2R\left[1 - \sqrt{1 - (r_b/R)^2}\right], \tag{1}$$

where R is the radius of the two equal-sized NBs. When $(r_b/R)^2$ is small, we have

$$\Delta x(r_b) \approx r_b^2/R. \tag{2}$$

Denoting the average radial velocity at radius r as $u_r(r)$, continuity for the incompressible liquid surrounding the capillary bridge gives[14]

$$2\pi r_b \Delta x(r_b) u_r(r_b) = 2\pi r \Delta x(r) u_r(r). \tag{3}$$

Substituting the expressions of Δx [i.e., Eq. (2)] into Eq. (3), we obtain

$$u_r(r) = \frac{dr}{dt} = \frac{r_b^3}{r^3}\frac{dr_b}{dt}. \tag{4}$$

2. Momentum conservation

The density and viscosity of gas in NBs are usually negligible compared to those of the surrounding liquid. In this case, the liquid near the capillary bridge can escape radially without significant axial velocity gradients, and the dominant velocity gradients are in the radial direction.[13] Accordingly, we substitute Eq. (4) into the axisymmetric NS equation,[22]

$$\frac{\partial u_r}{\partial t} + u_r\frac{\partial u_r}{\partial r} = -\frac{1}{\rho}\frac{\partial P}{\partial r} + \nu_L\left[\frac{1}{r}\frac{\partial}{\partial r}\left(r\frac{\partial u_r}{\partial r}\right) - \frac{u_r}{r^2}\right], \tag{5}$$

where P, ρ, and ν_L are the liquid pressure, density, and kinematic viscosity, respectively. Integrating Eq. (5) from a quiescent point far away where $P = P_\infty$ up to the capillary bridge radius r_b where $P = P(r_b)$, we obtain

$$\left(\frac{dr_b}{dt}\right)^2 + \frac{r_b}{2}\frac{d^2 r_b}{dt^2} = \frac{2\nu_L}{r_b}\frac{dr_b}{dt} + \frac{P(r_b) - P_\infty}{\rho}. \tag{6}$$

To determine the boundary condition $P(r_b)$ in Eq. (6), we denote the normal stress in the liquid near the capillary bridge and pointing radially outward from the symmetric axis as σ_{rr}. For an incompressible liquid with constant density and viscosity,[22]

$$\sigma_{rr} = -P(r) + 2\eta_L \frac{\partial u_r}{\partial r}, \tag{7}$$

where η_L is the dynamic viscosity of liquid. Accordingly, the net stress acting at the capillary bridge surface is

$$\sigma_{net} = P_B + \Delta P + \sigma_{rr}(r_b), \tag{8}$$

where P_B is the pressure of gas within the coalescing NBs and ΔP is the Laplace pressure in the bridge region. The Laplace pressure is the driving force for the capillary bridge expansion, which is given by

$$\Delta P = \gamma\left(\frac{1}{r_L} - \frac{1}{r_b}\right), \tag{9}$$

where γ is the liquid–vapor surface tension, and r_L and r_b are the principal radii of curvature at the bridge minimum, as depicted in Fig. 1. If there is no mass transfer across the NB surface, the net stress given by Eq. (8) should be zero; therefore,

$$P(r_b) = P_B + 2\eta_L \left.\frac{\partial u_r}{\partial r}\right|_{r=r_b} + \left(\frac{\gamma}{r_L} - \frac{\gamma}{r_b}\right). \tag{10}$$

Far from the bridge region, the NB surface can be considered static. Hence, the Laplace pressure across the bubble surface far from the bridge region is $P_B - P_\infty = 2\gamma/R$. Substituting this relation and Eq. (4) into Eq. (10), we obtain the boundary condition

$$P(r_b) - P_\infty = -\frac{6\eta_L}{r_b}\frac{dr_b}{dt} + \left(\frac{2\gamma}{R} + \frac{\gamma}{r_L} - \frac{\gamma}{r_b}\right). \tag{11}$$

Substituting Eq. (11) into Eq. (6), the result from momentum conservation becomes

$$\rho\left(\frac{dr_b}{dt}\right)^2 + \rho\frac{r_b}{2}\frac{d^2 r_b}{dt^2} + \frac{4\eta_L}{r_b}\frac{dr_b}{dt} = \frac{2\gamma}{R} - \frac{\gamma}{r_b} + \frac{\gamma}{r_L}. \tag{12}$$

3. The principal radius r_L at the bridge minimum

To solve the governing equation for $r_b(t)$, one needs to know the principal radius r_L at the bridge minimum as a function of r_b. In the study of the coalescence of millibubbles, Thoroddsen *et al.* suggested $r_L(r_b) \approx \Delta x(r_b)$.[15] Using this estimation, we set $r_L(r_b) = c\Delta x(r_b)$, where c is a dimensionless constant of the order unity. With this expression for r_L, the governing equation for $r_b(t)$ becomes

$$\rho\left(\frac{dr_b}{dt}\right)^2 + \rho\frac{r_b}{2}\frac{d^2 r_b}{dt^2} + \frac{4\eta_L}{r_b}\frac{dr_b}{dt} = \gamma\left[\frac{2}{R} - \frac{1}{r_b} + \frac{0.5/c}{R\left(1 - \sqrt{1 - (r_b/R)^2}\right)}\right]. \tag{13}$$

Rearranging Eq. (13), we obtain

$$\frac{\rho R^3}{\gamma}\left(\frac{d(r_b/R)}{dt}\right)^2 + \frac{\rho R^3}{\gamma}\frac{r_b}{2R}\frac{d^2(r_b/R)}{dt^2} + 4\frac{\eta_l R}{\gamma}\frac{1}{r_b/R}\frac{d(r_b/R)}{dt} = 2 - \frac{1}{r_b/R} + \frac{0.5/c}{1 - \sqrt{1 - (r_b/R)^2}}. \tag{14}$$

Denoting the characteristic inertial time $\tau_{inert} = \sqrt{\rho R^3/\gamma}$, the characteristic viscous time $\tau_{visc} = \eta_L R/\gamma$, and the dimensionless bridge radius $\tilde{r}_b = r_b/R$, the governing equation for $\tilde{r}_b(t)$ becomes

$$\left(\tau_{inert}\frac{d\tilde{r}_b}{dt}\right)^2 + \tau_{inert}^2\frac{\tilde{r}_b}{2}\frac{d^2\tilde{r}_b}{dt^2} + 4\tau_{visc}\frac{1}{\tilde{r}_b}\frac{d\tilde{r}_b}{dt} = 2 - \frac{1}{\tilde{r}_b} + \frac{0.5/c}{1 - \sqrt{1 - \tilde{r}_b^2}}. \tag{15}$$

B. The scaling laws for $r_b(t)$

If the coalescence dynamics of NBs is dominated by the inertial stress [i.e., the first term on the left hand side of Eq. (15)] or the viscous stress [i.e., the third term on the left hand side of Eq. (15)], we obtain particular cases of the general equation (15). In this case, one can estimate the expansion speed of the capillary bridge from the scaling laws for $r_b(t)$ in different dynamic regimes.

The bubble coalescence begins in the inertially limited viscous (ILV) regime where the dynamics is dominated by the viscous stress of gas within the bubble and the scaling law for $r_b(t)$ is given by[14]

$$r_b/R = C_0(\gamma/\eta_g R)t, \tag{16}$$

where C_0 is a constant of order unity and η_g is the viscosity of gas in the bubble. Equation (16) indicates $r_b \propto t$ and the bridge expands very fast (since η_g is usually very small) in the ILV regime. Equation (15) is not applicable in the ILV regime.

After starting in the ILV regime, the dynamics can transition into a second regime in which Eq. (15) is applicable. If the coalescence in the second regime is dominated by the viscous stress in the surrounding liquid, Eq. (15) can be simplified to

$$4\tau_{visc}\frac{1}{\tilde{r}_b}\frac{d\tilde{r}_b}{dt} \approx \frac{1}{c\tilde{r}_b^2}. \tag{17}$$

Equation (17) is valid for small $\tilde{r}_b$ such that the right hand side of Eq. (15) is dominated by the last term in Eq. (15). Integrating Eq. (17) gives the scaling law for $r_b(t)$ in the liquid viscous regime,

$$r_b/R = (1/2c)^{0.5}\sqrt{t/\tau_{visc}}. \tag{18}$$

Similarly, if the coalescence is dominated by the inertial stress in the surrounding liquid, Eq. (15) can be simplified to

$$\left(\tau_{inert}\frac{d\tilde{r}_b}{dt}\right)^2 \approx \frac{1}{c\tilde{r}_b^2}. \tag{19}$$

Equation (19) is also only valid for small $\tilde{r}_b$. Accordingly, the scaling law for $r_b(t)$ in the liquid inertial regime is

$$r_b/R = (4/c)^{0.25}\sqrt{t/\tau_{inert}}. \tag{20}$$

Equations (18) and (20) indicate that in both the liquid viscous regime and liquid inertial regime, the bubble coalescence scales as $r_b \propto \sqrt{t}$ with only a difference in their characteristic timescales,

and the proportionality constant is of order unity. These scaling laws derived from Eq. (15) are consistent with the existing theories for drop coalescence and bubble coalescence.[14,15] Furthermore, the recent experimental study on the coalescence of millibubbles shows the crossover from the viscous regime to inertial regime occurs when the Ohnesorge number ($Oh = \eta_L/\sqrt{\rho\gamma R}$) is close to 0.3.[14] In Secs. III and IV, we will use MD simulations to investigate if the scaling laws and the crossover Oh number found from the continuum-based theoretical model and experiments on millibubbles are still applicable to NBs.

III. MD SIMULATION OF COALESCENCE OF NBs

A. The MD model

As depicted in Fig. 2, the typical MD model system contains two 60-nm Ne NBs coalescing in saturated liquid Ar at a temperature of 85 K. A vapor Ar phase is included in the simulation box allowing for the liquid volume expansion during the coalescence process. The periodic boundary conditions (PBCs) are applied in all three directions. The thickness of the liquid domain between the liquid–vapor interface and the NB surface is chosen so that the coalescence dynamics is almost unaffected by the finite size of the liquid domain. All interatomic interactions in the MD model are described by the truncated and shifted Lennard-Jones (LJ) potential with parameters given in Table I. The cutoff distance for all LJ interactions is 10.9 Å. The potential parameters for Ar–Ne interactions are chosen to reduce the solubility of the model gas Ne in liquid Ar so that the amount of gas molecules that diffuse across the NB surface is negligible in the course of the NB coalescence process. In all MD simulations, we use a velocity Verlet algorithm[23] with a time step size of 5 fs to integrate the equations of motions. The long-range corrections to the pressure and potential energy are not considered in our MD model. All MD simulations are performed using the LAMMPS (Large-scale Atomic/Molecular Massively Parallel Simulator) simulation package.[24]

The MD simulation of the coalescence of two 60-nm Ne NBs in the model liquid Ar includes the following four steps:

Step 1: We first place a liquid slab of 11 950 542 Ar atoms in the middle of a simulation box, which has a length of 124 nm in the x-direction and a cross section area of 96 nm (y-direction) by 66 nm (z-direction). The PBCs are applied in three directions. We then carry out an NVT simulation for 2 ns to equilibrate the pure Ar system at a temperature of 85 K using a Nose–Hoover thermostat.[25] After the system reaches thermal equilibrium, the saturated liquid Ar coexistent with the saturated vapor Ar is present in the simulation box.

TABLE I. The LJ parameters used in the MD simulations.

	Ar–Ar[31]	Ne–Ne[31]	Ar–Ne
ε (meV)	10.3	4.05	4.05
σ (Å)	3.41	2.72	3.41

Step 2: Subsequently, a spherical region with a diameter of 60 nm is defined in the middle of the box. All Ar atoms in this region are removed, and 80 000 Ne atoms are inserted randomly into the region. The number of Ne atoms is determined using the Laplace pressure and the ideal gas equation. After the system with the inserted Ne atoms is equilibrated for 4 ns, a stable Ne bubble with a diameter of ~60 nm is generated at the middle of the simulation box. The equilibrated system is then duplicated in the z-direction to generate two identical 60-nm Ne bubbles in saturated liquid Ar. The separation between two Ne NBs is ~6 nm. The total number of atoms in the model fluid system is 19 428 660.

Step 3: To make the two Ne NBs approach each other and coalesce, we add instantaneous z-direction velocities of ± 50 m/s to Ne atoms in the bottom/top NB every 250 ps for a total of 1 ns. Afterward, we equilibrate the system for an additional 3 ns to stabilize the NBs and the two liquid–vapor interfaces in the model system. Subsequently, five more instantaneous velocities of ± 25 m/s were added to the bottom/top NB every 30 ps for a total of 120 ps. The magnitude of the velocity added to the NBs is small enough to avoid evident deformation of the two NBs when they approach each other. The Nose–Hoover thermostat is always applied in this step to equilibrate the fluid system to a temperature of 85 K. At the end of the approaching process, the separation between two NBs is below 2 nm.

Step 4: When the two NBs are less than 2 nm apart from each other, we stop adding instantaneous velocities to NBs and turn off the thermostat. Subsequently, we carry out an NVE simulation in the fluid system for 3 ns. The two NBs are now in Brownian motion. When the Brownian movement of the two NBs brings them closer and they touch, coalescence begins. To clearly show the geometry

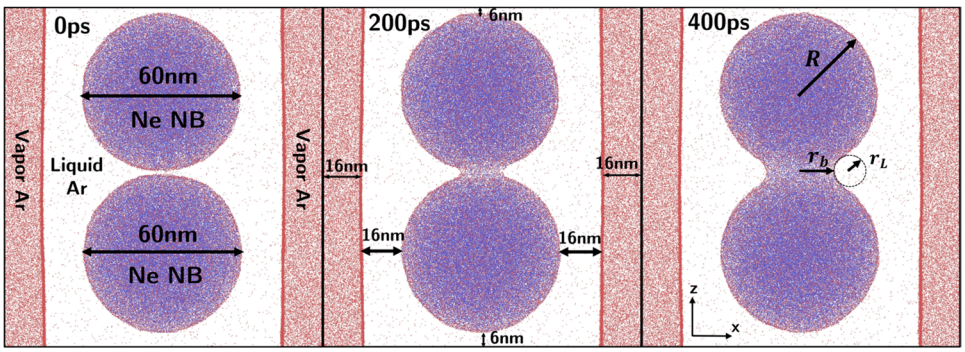

FIG. 2. Snapshots of 60-nm diameter Ne NBs coalescing in liquid Ar obtained in the MD model at 0 ps, 200 ps, and 400 ps after coalescence begins. The liquid Ar is hidden to clearly show the geometry of coalescing NBs. The red and blue dots in the snapshots represent the Ar and Ne atoms, respectively. A 16-nm-wide Ar vapor region is included in each side of the simulation box allowing for the liquid volume expansion during the coalescence process.

of NBs and the capillary bridge between them, we hide all liquid atoms in the snapshots shown in Fig. 2. In our MD model, an atom is defined as liquid if its potential energy is lower than half of that in saturated liquid Ar at a temperature of 85 K. This half-value cutoff for phase determination is arbitrary but faithfully reflects the phase transition occurring in the interfacial region. We have successfully used this method in our previous work to study the coalescence of nanodroplets.[26,27] To monitor the expansion of the capillary bridge during NB coalescence, we generate the snapshots of the model system every 10 ps. The bridge radius r_b as a function of t is obtained by measuring the width at the bridge minimum in each front-view projected snapshot and dividing the measured width by two.

By comparing the $r_b(t)$ obtained from MD simulations to the predictions from the governing equation for $r_b(t)$, i.e., Eq. (15), we will determine if the coalescence dynamics of NBs can be accurately described by the continuum-based theoretical model described in Sec. II. The two important parameters in Eq. (15) are τ_{inert} and τ_{visc}. To evaluate these two parameters, we need to know the density ρ, surface tension γ, and viscosity η_L of the model liquid Ar. All these properties are determined by the equilibrium MD (EMD) simulations described in Sec. III B.

B. Determination of fluid properties

We note that the properties of LJ fluids, in particular, the surface tension and liquid viscosity, are dependent on the cutoff distance. A cutoff distance of 10.9 Å used in our MD model will lead to lower surface tension and viscosity compared to those with longer cutoff distances. Our goal, however, is not to study Ar/Ne fluids specifically, but the coalescence dynamics of NBs in general. For this purpose, the cutoff distance of 10.9 Å is simply a part of the model fluid definition. Therefore, the following calculation results are specifically for the model LJ fluids with a cutoff distance of 10.9 Å.

1. Determination of density and surface tension

To determine the density ρ and surface tension γ of the model liquid Ar, we place a liquid slab of 26 714 Ar atoms at the center of a simulation box and randomly insert 2670 Ne atoms on two sides of the liquid slab, as shown in Fig. 3(a). The length of the simulation box in the x, y, and z directions is 50 nm, 10 nm, and 10 nm, respectively. The box size is fixed during the EMD simulation, and PBCs are applied in all three directions. The number of Ne atoms is determined using the density of Ne gas in the 60-nm NB described in Sec. III A. We equilibrate the system at a temperature of 85 K for 4 ns using the Nose–Hoover thermostat. After the system reaches equilibrium, liquid Ar sandwiched by a gas mixture of Ne and saturated vapor Ar is present in the simulation box. The thermostat is then turned off, and an NVE simulation is carried out for 2 ns to determine the distribution of Ar density (ρ_{Ar}), Ne density (ρ_{Ne}), and normal (P_N) and tangential (P_T) pressure tensor along the x direction, as shown in Fig. 3. From the Ar density at the center of the liquid slab, we find $\rho = 1360 \pm 3$ kg/m^3. The liquid–gas surface tension γ is determined using the mechanical definition according to Irving and Kirkwood,[28,29]

$$\gamma = \frac{1}{2}\int_0^{L_x} [P_N(x) - P_T(x)]dx, \tag{21}$$

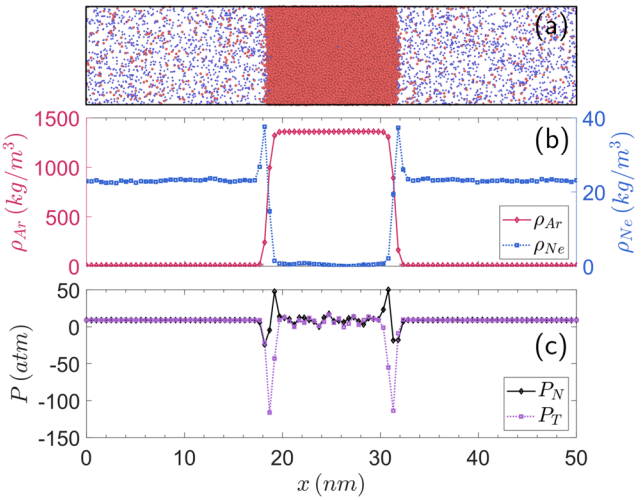

FIG. 3. (a) Snapshot of liquid Ar coexisting with the gas mixture of Ar and Ne. The red and blue dots in the snapshots represent the Ar and Ne atoms, respectively. The density of Ne is equal to the Ne gas density in a 60-nm diameter NB. (b) Density profiles for Ar (ρ_{Ar}) and Ne (ρ_{Ne}). (c) Normal (P_N) and tangential (P_T) pressure profiles.

where L_x is the length of simulation box in the x direction. Using P_N and P_T obtained from the MD simulation, we find $\gamma = 0.011 \pm 0.001$ N/m.

To study the NB size effects on the coalescence dynamics, we will gradually vary the NB diameter from 60 nm to 30 nm in MD simulations. As the NB size decreases, the Laplace pressure increases, which leads to a higher Ne gas density in NBs. To investigate how the Ne gas density would affect the density ρ and surface tension γ of the model liquid Ar, we vary the Ne gas density from 0 kg/m^3 to 46 kg/m^3 and carry out similar EMD simulations as described above. The MD simulation results show there is no discernible change in the density and surface tension of the model liquid Ar in the range of Ne density simulated. This result can be attributed to the small interaction strength chosen for Ar–Ne, which leads to low solubility of the Ne gas in liquid Ar,[30] as shown in Fig. 3(b).

2. Determination of viscosity

To evaluate the viscosity η_L of the model liquid Ar at $T = 85$ K and $\rho = 1360$ kg/m^3, we carry out a separate EMD simulation in a cubic simulation box containing 2563 model Ar molecules. The box side length is fixed at 5 nm such that the density of Ar equals to 1360 kg/m^3. The PBCs are applied in all three directions. A Nose–Hoover thermostat is applied for 2 ns to equilibrate the model liquid Ar to a temperature of 85 K. After the system reaches the thermal equilibrium, we turn off the thermostat and carry out the simulation in a microcanonical ensemble for 80 ns to calculate the autocorrelation function of the pressure tensor in the model liquid Ar, as shown in Fig. 4. The viscosity is then determined from the Green–Kubo relation,[31]

$$\eta = \frac{V}{k_B T}\int_0^{\infty} dt\langle P_{\alpha\beta}(t)\cdot P_{\alpha\beta}(0)\rangle, \tag{22}$$

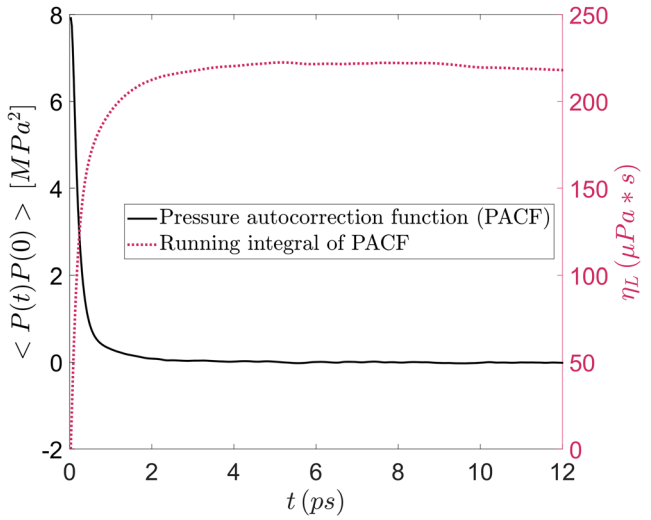

FIG. 4. The pressure-tensor autocorrelation function (PACF) and the running integral of the PACF of the model liquid Ar at a temperature of 85 K and a density of 1360 kg/m^3.

where

$$P_{\alpha\beta} = \frac{1}{V}\left(\sum_i m v_{i\alpha} v_{i\beta} + \sum_i \sum_{j>i} r_{ij_\alpha} f_{ij_\beta}\right). \tag{23}$$

In Eqs. (22) and (23), k_B is the Boltzmann constant, V and T are the volume and temperature of the system, respectively, P is the pressure tensor, m is the mass of fluid atom, v_i is the translational velocity of ith molecule, r and f are the interatomic separation and force, respectively, the subscripts α and β denote the vector component, t is the time, and $\langle\cdots\rangle$ denotes the ensemble average. From the plateau of the running integral of $\langle P(t)P(0)\rangle$ shown in Fig. 4, we find $\eta_L = 220 \pm 5\ \mu$Pa s for the model liquid Ar. Using the similar method, we find the viscosity η_g of the gas mixture within the 60-nm NB is 19.9 μPa s.

The calculated properties of the model fluid will be used in Sec. IV to analyze the coalescence dynamics of NBs obtained from MD simulations.

IV. MODELING RESULTS

A. Representative modeling results

In this section, we show the representative continuum and molecular modeling results of coalescence of two 60-nm diameter Ne NBs in the model liquid Ar at a temperature of 85 K. Using $R = 30$ nm and the fluid properties obtained in Sec. III B, we find the characteristic time $\tau_{inert} = 1.83$ ns and $\tau_{visc} = 0.63$ ns for the 60-nm NBs in the model fluid system. Substituting these two time constants into Eq. (15), we obtain the theoretical prediction of $r_b(t)$.

1. Comparison of $r_b(t)$

In Fig. 5(a), we compare the $r_b(t)$ measured directly from the MD simulation to that obtained from the continuum-based theoretical model.

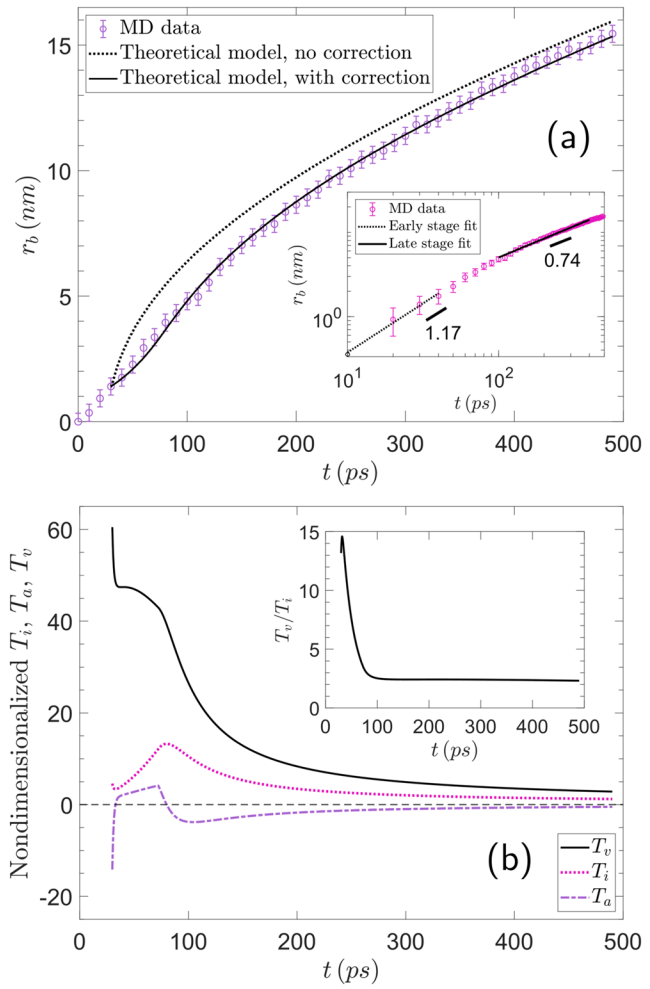

FIG. 5. (a) $r_b(t)$ obtained from the MD simulation (scatters), Eq. (15) with $c = 1.0$ (dashed line), and Eq. (25) with $c = 1.0$ (solid line) for the coalescence of two 60-nm Ne NBs in liquid Ar ($Oh = 0.33$). The inset shows the same axis parameters on the logarithmic scale to extract the early and later time slopes. (b) Inertial, acceleration, and viscous terms from the governing equation over t. The inset is the ratio of the viscous and inertial terms over time t.

Recent studies on the coalescence of millibubbles[14] show the bubble coalescence starts in the ILV regime in which $r_b \propto t$. The logarithmic plot of the MD data [see the inset of Fig. 5(a)] shows that at early time (10 ps < t < 40 ps) of the coalescence, $r_b \propto t^{1.17}$. To investigate if the early time dynamics of the NB coalescence is in the ILV regime, we fit the MD data at the first 40 ps with a linear function and obtain the bridge expansion speed of ~35.5 m/s. This value is considerably lower than the theoretical expansion speed $dr_b/dt \approx \gamma/\eta_g \approx 550$ m/s in the ILV regime predicted by Eq. (16). Hence, we believe the simulated NB coalescence is already out of the ILV regime a few tens of ps after coalescence begins.

After the NB coalescence passes the ILV regime, the continuum-based theoretical model described in Sec. II can be applied for the analysis of the MD data. To solve the governing equation, i.e., Eq. (15), for $r_b(t)$, we use the finite difference method

with the initial conditions $r_b(t = 30\ \text{ps}) = 1.3$ nm and dr_b/dt $(t = 30\ \text{ps}) = 35.5$ m/s directly taken from the MD simulation results. We choose $t = 30$ ps as our initial time to ensure the coalescence dynamics is already out of the ILV regime. We find that a good match between the prediction from Eq. (15) and the MD results is obtained when the dimensionless constant c in Eq. (15) is 1.0. In this case, the theoretical prediction [dashed line in Fig. 5(a)] has generally a reasonable agreement with the MD data. However, Fig. 5(a) also shows the theoretical prediction significantly overestimates the expansion speed at the early stage (30 ps $< t <$ 100 ps) of the NB coalescence.

To investigate the aforementioned discrepancy at early time of coalescence, we recall the principal radii r_b and r_L at the bridge minimum shown in Fig. 1. In our theoretical model, $r_L(r_b) \approx \Delta x(r_b)$ is used to estimate r_L. From the relation $\Delta x(r_b) \approx r_b^2/R$ [see Eq. (2)], one can readily find that $\Delta x(r_b)$ is less than the size of the model Ar atom ($\sigma = 0.341$ nm) if r_b is smaller than 3.2 nm. The MD simulation results show r_b is below 3.2 nm until $t \approx 90$ ps. Hence, within 90 ps after coalescence begins, the principal radius r_L estimated from the continuum-based analysis is below the size of the model Ar atom, which is unphysical. The unrealistically small r_L leads to an unrealistically high curvature and Laplace pressure in the theoretical model, which results in an over-prediction of the expansion speed at the early stage (30 ps $< t <$ 100 ps) of the NB coalescence. Hence, we propose a corrected theoretical model in which the minimum $r_L(r_b)$ and $\Delta x(r_b)$ values are restricted to the size of the model Ar atom ($\sigma = 0.341$ nm).

Furthermore, if the principal radius of the liquid surface is comparable to the size of the fluid atom, the surface tension at these highly curved surfaces could significantly deviate from that at a flat surface.[32,33] To account for the curvature effects on the surface tension, we use the Helfrich expansion[33]

$$\tilde{\gamma} = \frac{\gamma(J,K)}{\gamma_0} = 1 - \delta J + \frac{k_1}{2\gamma_0}J^2 + \frac{k_2}{\gamma_0}K, \tag{24}$$

where γ is the surface tension of a curved surface, γ_0 is the surface tension of a flat surface, $J = 1/r_1 + 1/r_2$ is the total curvature, and $K = (r_1 r_2)^{-1}$ is the Gaussian curvature, where r_1 and r_2 are the principal radii of curvature. At the capillary bridge minimum, $r_1 = -r_b$ and $r_2 = r_L$. In Eq. (24), the three constants δ, k_1, and k_2 are the Tolman length,[34] the bending rigidity, and the rigidity constant associated with the Gaussian curvature, respectively. We carry out the MD simulation in a LJ fluid system with a cutoff distance of 10.9 Å at a temperature of 85 K. Using the LJ parameters of Ar, the cutoff distance and the temperature in the reduced LJ units are 3.2 and 0.71, respectively. For a LJ fluid with a reduced cutoff distance of 3.2, the values of δ, k_1, and k_2 in the reduced LJ units at a reduced temperature of 0.71 are −0.088, −0.592, and 0.375, respectively.[32] Using these constants in Eq. (24), we show in Fig. 6 the dependence of surface tension on r_b. When r_b is less than 6 nm, it is seen the surface tension at the bridge minimum is evidently lower than that at the flat surface. If we treat the surface tension as a constant and use the value at the flat surface in the theoretical model, therefore, we will overestimate the driving force for bridge expansion and over-predict the expansion speed when r_b is small. Because we use the restriction $r_L(r_b) \geq 0.341$ nm in the corrected theoretical model, it is shown in Fig. 6 that the surface tension will not further decrease when $r_b < 3.2$ nm.

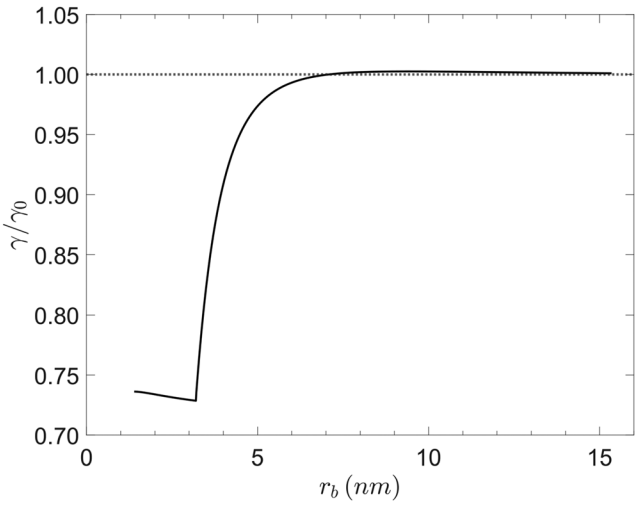

FIG. 6. Normalized surface tension at the bridge of two coalescing 60-nm NBs as a function of r_b.

By incorporating Eq. (24) into Eq. (15), we obtain the corrected governing equation for $r_b(t)$,

$$\left(\tau_{inert}\frac{d\tilde{r}_b}{dt}\right)^2 + \tau_{inert}^2\frac{\tilde{r}_b}{2}\frac{d^2\tilde{r}_b}{dt^2} + 4\tau_{visc}\frac{1}{\tilde{r}_b}\frac{d\tilde{r}_b}{dt} = 2 - \frac{\tilde{\gamma}}{\tilde{r}_b} + \frac{0.5\tilde{\gamma}/c}{1-\sqrt{1-\tilde{r}_b^2}}. \tag{25}$$

In the corrected theoretical model, we (1) take into account the curvature-dependent liquid–vapor surface tension and (2) restrict $r_L(r_b)$ to no smaller than the size of the Ar atom. As shown in Fig. 5(a), within 500 ps after coalescence begins, r_b increases to ~16 nm and the prediction from the corrected theoretical model (solid line) agrees with the MD data very well. Moreover, after taking into account the curvature effects on the surface tension in Eq. (16), the theoretical prediction for the expansion speed in the ILV regime is reduced to about 400 m/s, which is still significantly higher than the bridge expansion speed (35.5 m/s) obtained from the first 40 ps of our MD data. This result confirms that the coalescence dynamics is out of the ILV regime at $t = 30$ ps.

2. Comparison of the scaling laws

Once a crossover occurs out of the ILV regime into a second regime dominated by either liquid viscosity or liquid inertial, the theoretical model predicts the growth of the bridge radius follows the scaling law $r_b \propto t^{0.5}$. Certainly, this scaling law is only valid when the surface tension is a constant. However, it is shown in Fig. 6 that the surface tension cannot be considered as a constant until $r_b >$ 6 nm. Accordingly, we use $r_b = 6$ nm as the lower limit for the fit to the MD data in the later time. Furthermore, from the study of the coalescence dynamics of millibubbles, Thoroddsen *et al.* showed that the scaling law $r_b \propto t^{0.5}$ is valid for $r_b/R < 0.45$.[15] Therefore, $r_b = 13.5$ nm is used as the upper limit for the fit to the MD data in the later time. Out of these two limits, the $r_b \propto t^{0.5}$ scaling laws for the viscous-dominated regime and inertial-dominated regime are not valid. Applying the power function fit ($r_b \propto t^n$) to the MD data between the aforementioned lower and upper limits, we obtain

n = 0.74, as shown in the inset of Fig. 5(a). This value is considerably higher than n = 0.5 in the viscous-dominated or inertial-dominated regime.

To understand the high exponent found in the MD data, we calculate the Ohnesorge number for the 60-nm NBs in the model fluid system. Using the fluid properties found in Sec. III, we obtain $Oh = 0.33$. The experimental study on the coalescence of millibubbles shows the crossover from the liquid viscous regime to the liquid inertial regime occurs when Oh is close to 0.3.[14] If this result is also applicable to NBs, $Oh = 0.33$ indicates the coalescence dynamics of NBs at later time is in a crossover regime where neither viscous stress nor inertial stress in the surrounding liquid dominates the coalescence dynamics. To verify this prediction, we define the three terms from left to right on the left hand side of Eq. (25) as the inertial term T_i, acceleration term T_a, and viscous term T_v, respectively, and calculate T_i, T_a, and T_v as a function of time during NB coalescence. Since the prediction from Eq. (25) closely follows our MD results, the ratio T_v/T_i calculated from Eq. (25) will be a good indicator of the significance of viscous and inertial stresses in the surrounding liquid on coalescence dynamics at later time.

It is shown in Fig. 5(b) that T_i, T_a, and T_v at later time all decay with time, and the magnitude of T_a is much smaller than T_i and T_v. The inset of Fig. 5(b) shows T_v is consistently higher than T_i, and after $t > 100$ ps, the ratio T_v/T_i is nearly a constant around 2.4. The ratio between T_v and T_i at later time confirms that neither viscous nor inertial stresses are negligible. Therefore, the coalescence dynamics of the 60-nm diameter NBs is not in the viscous-dominated or inertial-dominated regime. In such a transition regime, $r_b(t)$ obtained from Eq. (25) predicts $r_b \propto t^{0.68}$, which has a reasonable agreement with $r_b \propto t^{0.74}$ found from the MD data. This explains why the growth of the bridge radius does not follow the scaling law $r_b \propto t^{0.5}$ at later time.

3. The size of fully merged equilibrium NB

The governing equation, i.e., Eq. (25), is derived based on the assumption that r_b/R is small and $r_L(r_b) \approx \Delta x(r_b)$. As r_b approaches and exceeds R during the coalescence, $r_L(r_b) \approx \Delta x(r_b)$ will not be a good approximation and Eq. (25) will be invalid. Hence, it is not suitable to use Eq. (25) to predict r_b for the whole NB coalescence process. Nevertheless, we can still predict the size of fully merged NB using the following theoretical analysis.

The pressure of gas within the NB before coalescence begins is given by

$$P_B = P_\infty + \frac{2\gamma}{R} = P_{Ne} + P_{Ar}, \tag{26}$$

where P_{Ne} and P_{Ar} are the partial pressure of Ne and Ar in the gas mixture within the NB, respectively. When our model fluid system is at thermal equilibrium, P_∞ and P_{Ar} in Eq. (26) equal to the saturated pressure of Ar at a flat and a curved liquid surface, respectively. Plugging the fluid properties obtained in Sec. III and R = 30 nm into the Kelvin equation,[35] we find there is only ~3% difference between P_∞ and P_{Ar}. Furthermore, the Laplace pressure $2\gamma/R$ is about six times of P_∞ in our model fluid system. Using $P_\infty \approx P_{Ar}$ and $2\gamma/R \gg P_\infty$, Eq. (26) is reduced to

$$\frac{2\gamma}{R} = P_{Ne} = \frac{N_{Ne}}{V} k_B T, \tag{27}$$

where we used the ideal gas approximation for gas Ne, with N_{Ne} being the number of Ne atoms in a single NB before coalescence begins. Assuming no Ne atoms diffuse across the NB surface during the coalescence process, we apply the same analysis to the fully merged NB with a new radius R_n and volume V_n and obtain

$$\frac{2\gamma}{R_n} = \frac{2N_{Ne}}{V_n} k_B T. \tag{28}$$

From the combination of Eqs. (27) and (28), one can readily find $R_n = \sqrt{2}R$. Note that this relation for NB is different from $R_n = \sqrt[3]{2}R$ that is often found in the coalescence of microbubbles or millibubbles.[11] For microbubbles or millibubbles, the Laplace pressure is usually much smaller than the pressure in liquid ($2\gamma/R \ll P_\infty$). Accordingly, the gas pressure within microbubbles or millibubbles is always close to the pressure (P_∞) in the surrounding liquid, which leads to $R_n = \sqrt[3]{2}R$.

As shown in Fig. 7, after the two 60-nm NBs fully merge into a bigger NB at the end of our MD simulation, r_b/R approaches 1.42 that is consistent with the theoretical prediction $R_n = \sqrt{2}R$. At $t \approx 4$ ns, one can see a small dip in the $r_b(t)$ curve, which is caused by the transient convex liquid–vapor interfaces. During the coalescence process, the bridge expansion pushes the surrounding liquid in the radial direction resulting in a considerable curvature at the two originally flat liquid–vapor interfaces at $t \approx 4$ ns, as shown in Fig. 7. The curved surface added an extra Laplace pressure to liquid, which slows down the bridge expansion. The convex liquid–vapor interfaces return to almost flat again at $t \approx 8$ ns and remain flat in the rest of the coalescence process, as shown in Fig. 7. No oscillations of merged NB are found in our MD model. This result is consistent with our theoretical prediction that the liquid viscosity has a more significant effect on NB coalescence.

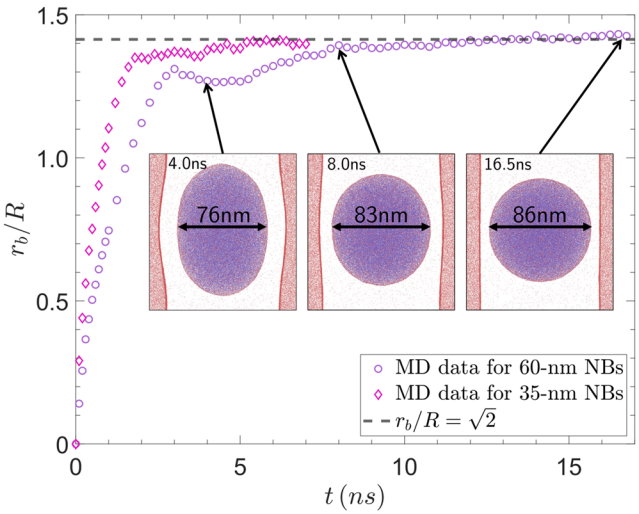

FIG. 7. Normalized bridge radius r_b/R of two coalescing 60-nm and 35-nm NBs obtained from MD simulations. Uncertainties are smaller than the symbols denoting the MD data. The horizontal dashed line represents the maximum normalized radius R_n of the fully coalesced NBs.

B. Effects of NB size on coalescence dynamics

Using the similar method, we study the coalescence dynamics of NBs with a diameter ranging from 30 nm to 60 nm. For all NB sizes, the MD simulation results show the diameter of fully merged NB is about $\sqrt{2}$ of that of the original NB (see Fig. 7 for results of 35-nm and 60-nm NBs), and the merged NBs do not oscillate indicating significant viscous effects on NB coalescence. For each NB size, we adjust the value of dimensionless constant c in Eq. (25) to obtain a good agreement between the prediction from the continuum-based theoretical model and the MD simulation results. As shown in Fig. 8(a) through 8(e), the optimized c value increases with decreasing NB size. Nevertheless, they all fall in the range of 1.2 ± 0.2, which indicates $r_L(r_b) \approx \Delta x(r_b)$ is a reasonable approximation for the principal radius of the capillary bridge between two NBs. With the optimized c values, Figs. 8(a)–8(e) show theoretical predictions have generally a good agreement with MD results for all NB sizes.

As the NB diameter decreases from 60 nm to 30 nm, the corresponding Oh increases from 0.33 to 0.46. A higher Oh implies that the viscous stress in liquid has a more significant effect on NB coalescence. Accordingly, one would expect the coalescence dynamics to transit toward the viscous-dominated regime and the scaling exponent at later time to approach 0.5 as NB size decreases. However, we do not see such a trend from our MD data for Oh ranging from 0.33 to 0.46. For all NB sizes studied, a fit to the MD data at early time ($10\ \text{ps} < t < 40\ \text{ps}$) of coalescence gives $r_b(t) \propto t^{1.03 \pm 0.14}$, and a fit to the MD data at later time gives $r_b(t) \propto t^{0.76 \pm 0.04}$, as shown in Figs. 8(f)–8(j). In all cases, we define the moment when $r_b/R = 0.45$ as the upper limit of the later time of coalescence and the moment when $\gamma = 0.99\gamma_0$ as the lower limit.

An almost constant scaling exponent at later time could be caused by the narrow range of Oh studied in this work. To find how the relative significance of viscous stress and inertial stress changes with Oh, we calculate T_v and T_i for each NB size from Eq. (25). Similar to the inset of Fig. 5(b), we find the ratio T_v/T_i in each case is nearly a constant at later time of coalescence. Figure 9 shows the ratio T_v/T_i increases from 2.4 to 6.2 as Oh increases from 0.33 to 0.46. Even for the highest Oh in this study, $T_v/T_i = 6.2$ indicates that the inertial term is non-negligible on the left hand side of Eq. (25). Hence, the scaling law $r_b \propto t^{0.5}$ is still not applicable for the coalescence of 30-nm diameter NBs. On the other hand, the increase of T_v/T_i from 2.4 to 6.2, indeed, shows the viscous term is much more significant in the case with 30-nm diameter NBs. Using Eq. (25), we find the theoretical prediction of the scaling exponent in the later time of coalescence of 30-nm diameter NBs is ~0.61, which is apparently lower than 0.73 found from the MD simulation [see Fig. 8(f)]. In fact, deviations between the theoretical prediction and the MD results become more visible for smaller NBs, as shown in Figs. 8(a) and 8(b).

There are two reasons that might lead to a higher than expected scaling exponent in the coalescence of smaller NBs. First, as the NB

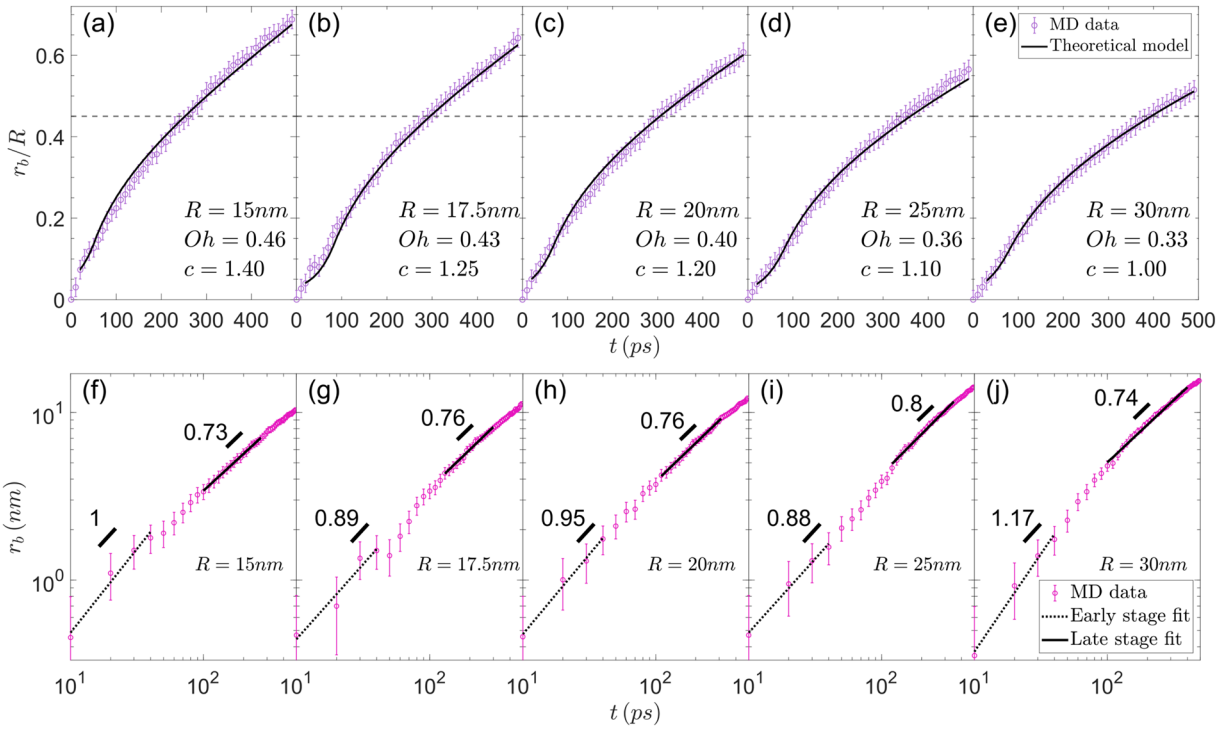

FIG. 8. [(a)–(e)] Normalized bridge radius r_b/R for NB diameters ranging from 30 nm to 60 nm obtained from MD simulations (scatters) and Eq. (25) (solid lines). The horizontal dashed line show the upper limit $r_b/R = 0.45$ for the power fit at later time of NB coalescence. The NB radius R, Oh, and the optimized c are listed for each NB size. [(f)–(j)] Logarithmic bridge radius $\log(r_b)$ vs $\log(t)$ at early and later time.

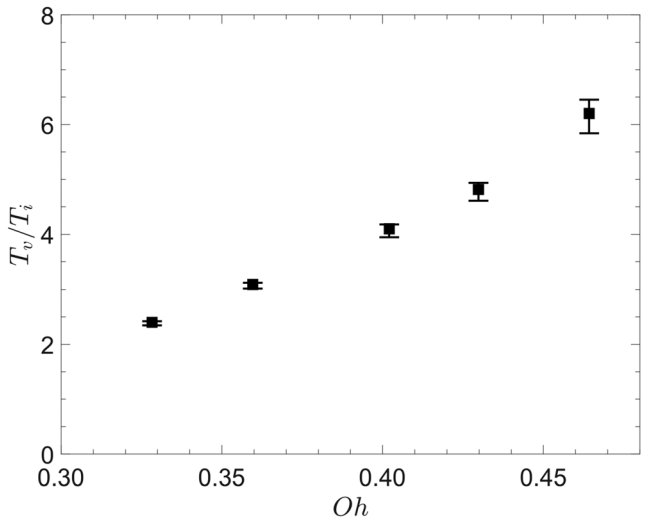

FIG. 9. Dependence of the ratio T_v/T_i at later time of coalescence on Oh calculated from Eq. (25). The square symbols are the average ratios in the range between the lower and upper limits of the later time of coalescence. The error bars represent the minimum and maximum T_v/T_i ratios in that range.

size gets smaller, the range of MD data that can be used for power function fit at later time decreases. For the case with 30-nm diameter NBs, only $r_b(t)$ ranging from 4.0 nm to 6.7 nm are within the lower and upper limits of the later time of coalescence. Moreover, it is more difficult to visually identify the bridge interface for smaller NBs in the MD model, which leads to a less accurate measurement of $r_b(t)$ in the MD model. It is challenging to obtain a reliable slope in such a narrow range of r_b with relatively large uncertainties. Second, we estimate the principal radius r_L at the bridge as $r_L(r_b) = c\Delta x(r_b)$ in the theoretical model. As r_b changes from 4.0 nm to 6.7 nm during the coalescence of two 30-nm diameter NBs, $\Delta x(r_b)$, which can be approximated as r_b^2/R, is only about 1 or 2 nm, i.e., the size of a few fluid atoms. In this case, r_L may not vary continuously as a linear function of Δx. If r_L is a more complex function of Δx for smaller NBs, the theoretical model will give a different scaling law at later time of coalescence. These complexities in the modeling of smaller NBs might be the reason for the small discrepancy between the theoretical predictions and MD results.

To observe a clear crossover from the viscous-dominated regime and the inertial-dominated regime, one should study the coalescence dynamics of a much wider range of NB sizes. However, the computational cost for MD simulations of NBs of hundreds of nm is prohibitive with the current computing power. One possible solution to this problem in the future is that one can fix the NB size at tens of nm and change Oh by replacing the liquid Ar with other liquids having a wide range of viscosity, density, and surface tension.

V. CONCLUSIONS

Using the combination of continuum-based theoretical model and MD simulations, we studied the coalescence dynamics of NBs of 30 nm–60 nm diameter. The coalescence of NBs is characterized by the expansion speed of the capillary bridge between two coalescing NBs. To understand the evolution of the capillary bridge radius r_b obtained from MD simulations, we derived a governing equation for $r_b(t)$ from the axisymmetric NS equation. Our modeling results show the continuum-based theoretical prediction significantly overestimates the expansion speed at early time of NB coalescence. The discrepancy is mainly caused by the very large curvature at the capillary bridge between the coalescing NBs. Once we take into account the curvature-dependent liquid–vapor surface tension and restrict the minimum principal radius at the capillary bridge to the size of the Ar atom in the MD model, the theoretical prediction agrees with the MD data very well in both early time and later time of the coalescence process. The Laplace pressure across the NB surface is usually much greater than that in the liquid. As a result, the diameter ratio of fully merged NB to that before coalescence begins is about $\sqrt{2}$, which is different from the diameter ratio of $\sqrt[3]{2}$ for millibubbles and microbubbles. Due to significant viscous effects on NB coalescence, no oscillations of the merged NBs are observed for any NB sizes studied in this work.

The Oh of NBs studied in this work varies from 0.33 to 0.46. Using the governing equation derived from the NS equation, we calculated the relative significance of viscous stress and inertial stress in liquid surrounding the NBs during their coalescence. The calculation results show neither liquid viscosity nor liquid inertia dominates at the later time of coalescence. In this case, our modeling results show the scaling exponent in the scaling law $r_b \propto t^n$ is $n \approx 0.7$ at later times of NB coalescence. This value is considerably higher than $n = 0.5$ in the viscous-dominated regime or the inertial-dominated regime. To observe a clear crossover from the viscous-dominated regime and the inertial-dominated regime, it is imperative in the future to study the coalescence of NBs in other fluid systems that have a wide range of viscosity, density, and surface tension.

ACKNOWLEDGMENTS

This work was supported by NSF under Grant No. 1911434. Additionally, we would like to thank the Extreme Science and Engineering Discovery Environment (XSEDE) for providing us supercomputer resources for MD simulations.

DATA AVAILABILITY

The data that support the findings of this study are available from the corresponding author upon reasonable request.

REFERENCES

[1] M. Alheshibri, J. Qian, M. Jehannin, and V. S. J. Craig, "A history of nanobubbles," Langmuir **32**, 11086 (2016).
[2] H. Li, L. Hu, D. Song, and F. Lin, "Characteristics of micro-nano bubbles and potential application in groundwater bioremediation," Water Environ. Res. **86**, 844 (2015).
[3] A. Agarwal, W. J. Ng, and Y. Liu, "Principle and applications of microbubble and nanobubble technology for water treatment," Chemosphere **84**, 1175 (2011).
[4] R. Ahmadi, D. A. Khodadadi, M. Abdollahy, and M. Fan, "Nano-microbubble flotation of fine and ultrafine chalcopyrite particles," Int. J. Min. Sci. Technol. **24**, 559 (2014).
[5] S. Calgaroto, A. Azevedo, and J. Rubio, "Flotation of quartz particles assisted by nanobubbles," Int. J. Miner. Process. **137**, 64 (2015).

[6]W. Zhou, H. Chen, L. Ou, and Q. Shi, "Aggregation of ultra-fine scheelite particles induced by hydrodynamic cavitation," Int. J. Miner. Process. **157**, 236 (2016).
[7]B. A. Wills and K. Atkinson, "The development of minerals engineering in the 20th century," Miner. Eng. **4**, 643 (1991).
[8]J. B. Yianatos, L. G. Bergh, F. Díaz, and J. Rodríguez, "Mixing characteristics of industrial flotation equipment," Chem. Eng. Sci. **60**, 2273–2282 (2005).
[9]Z. Wu, H. Chen, Y. Dong, H. Mao, J. Sun, S. Chen, V. S. J. Craig, and J. Hu, "Cleaning using nanobubbles: Defouling by electrochemical generation of bubbles," J. Colloid Interface Sci. **328**, 10 (2008).
[10]C. F. Gurnham, "Aqueous wastes from petroleum and petrochemical plants, M. R. Beychok, John Wiley & Sons, Inc., New York (1967). 370 Pages, $ 12.75," AIChE J. **14**, 2 (1968).
[11]R. L. Stover, C. W. Tobias, and M. M. Denn, "Bubble coalescence dynamics," AIChE J. **43**, 2385 (1997).
[12]S. Orvalho, M. C. Ruzicka, G. Olivieri, and A. Marzocchella, "Bubble coalescence: Effect of bubble approach velocity and liquid viscosity," Chem. Eng. Sci. **134**, 205 (2015).
[13]Á. Moreno Soto, T. Maddalena, A. Fraters, D. van der Meer, and D. Lohse, "Coalescence of diffusively growing gas bubbles," J. Fluid Mech. **846**, 143 (2018).
[14]J. D. Paulsen, R. Carmigniani, A. Kannan, J. C. Burton, and S. R. Nagel, "Coalescence of bubbles and drops in an outer fluid," Nat. Commun. **5**, 1 (2014).
[15]S. T. Thoroddsen, T. G. Etoh, K. Takehara, and N. Ootsuka, "On the coalescence speed of bubbles," Phys. Fluids **17**, 1 (2005).
[16]C. Li, A.-M. Zhang, S. Wang, and P. Cui, "Formation and coalescence of nanobubbles under controlled gas concentration and species," AIP Adv. **8**, 015104 (2018).
[17]Y.-X. Chen, Y.-L. Chen, and T.-H. Yen, "Investigating interfacial effects on surface nanobubbles without pinning using molecular dynamics simulation," Langmuir **34**, 15360 (2018).
[18]S. Maheshwari, M. van der Hoef, X. Zhang, and D. Lohse, "Stability of surface nanobubbles: A molecular dynamics study," Langmuir **32**, 11116 (2016).
[19]Y. Liu and X. Zhang, "Molecular dynamics simulation of nanobubble nucleation on rough surfaces," J. Chem. Phys. **146**, 164704 (2017).
[20]Z. Huang, M. Su, Q. Yang, Z. Li, S. Chen, Y. Li, X. Zhou, F. Li, and Y. Song, "A general patterning approach by manipulating the evolution of two-dimensional liquid foams," Nat. Commun. **8**, 14110 (2017).
[21]C. R. Anthony, P. M. Kamat, S. S. Thete, J. P. Munro, J. R. Lister, M. T. Harris, and O. A. Basaran, "Scaling laws and dynamics of bubble coalescence," Phys. Rev. Fluids **2**, 083601 (2017).
[22]D. C. Wilcox, *Basic Fluid Mechanics*, 2nd ed. (DCW Industries, 2003).
[23]L. Verlet, "Computer 'experiments' on classical fluids. I. Thermodynamical properties of Lennard-Jones molecules," Phys. Rev. **159**, 98 (1967).
[24]S. Plimpton, "Fast parallel algorithms for short-range molecular dynamics," J. Comput. Phys. **117**, 1 (1995).
[25]D. J. Evans and B. L. Holian, "The nose-hoover thermostat," J. Chem. Phys. **83**, 4069 (1985).
[26]Z. Liang and P. Keblinski, "Coalescence-induced jumping of nanoscale droplets on super-hydrophobic surfaces," Appl. Phys. Lett. **107**, 143105 (2015).
[27]R. Bardia, Z. Liang, P. Keblinski, and M. F. Trujillo, "Continuum and molecular-dynamics simulation of nanodroplet collisions," Phys. Rev. E **93**, 053104 (2016).
[28]J. G. Kirkwood and F. P. Buff, "The statistical mechanical theory of surface tension," J. Chem. Phys. **17**, 338 (1949).
[29]J. P. R. B. Walton, D. J. Tildesley, J. S. Rowlinson, and J. R. Henderson, "The pressure tensor at the planar surface of a liquid," Mol. Phys. **48**, 1357 (1983).
[30]Z. Liang and P. Keblinski, "Molecular simulation of steady-state evaporation and condensation in the presence of a non-condensable gas," J. Chem. Phys. **148**, 064708 (2018).
[31]R. Scott, M. P. Allen, and D. J. Tildesley, "Computer simulation of liquids," Math. Comput. **57**, 442 (1991).
[32]Ø. Wilhelmsen, D. Bedeaux, and D. Reguera, "Tolman length and rigidity constants of the Lennard-Jones fluid," J. Chem. Phys. **142**, 064706 (2015).
[33]W. Helfrich, "Elastic properties of lipid bilayers: Theory and possible experiments," Z. Naturforsch. C **28**, 693 (1973).
[34]R. C. Tolman, "The effect of droplet size on surface tension," J. Chem. Phys. **17**, 333 (1949).
[35]R. von Helmholtz, "Untersuchungen über Dämpfe und Nebel, besonders über solche von Lösungen," Ann. Phys. **263**, 508 (1886).